ACS APPLIED ENERGY MATERIALS
Cite This: ACS Appl. Energy Mater. 2019, 2, 5472−5480
Article
www.acsaem.org

P-Substituted $Ba_{0.95}La_{0.05}FeO_{3-\delta}$ as a Cathode Material for SOFCs

Jiapeng Liu,[†] Jian Wang,[†] Alessio Belotti,[†] and Francesco Ciucci*[,†,‡]

[†]Department of Mechanical and Aerospace Engineering and [‡]Department of Chemical and Biological Engineering, The Hong Kong University of Science and Technology, Hong Kong, China

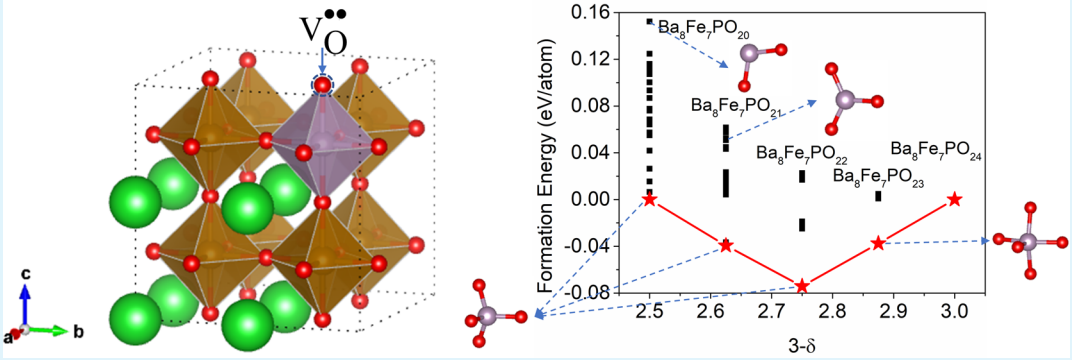

ABSTRACT: The need for clean and efficient energy conversion systems has stimulated tremendous research activities in the area of energy systems. Solid oxide fuel cells stand out because of their high efficiency and low emissions. In spite of the promise, to commercialize solid oxide fuel cells, the operating temperature needs to be reduced below 800 °C. Unfortunately, at such low temperatures the oxygen reduction reactions taking place at the cathode side of the solid oxide fuel cells are typically sluggish. Ferrites have recently shown that they can overcome this challenge. However, the conductivity of these materials is typically low. Here, we show by density functional theory calculations that substituting Fe in $Ba_{1-x}La_xFeO_{3-\delta}$ with P lowers both the O vacancy formation and vacancy migration energies and promotes the creation of PO_4 groups. These factors contribute to improving the diffusional properties and oxygen reduction reaction performance. We further successfully introduce P in the Fe-site of $Ba_{0.95}La_{0.05}FeO_{3-\delta}$ to make a novel cathode material, $Ba_{0.95}La_{0.05}Fe_{0.95}P_{0.05}O_{3-\delta}$. Consistently, we observe that $Ba_{0.95}La_{0.05}Fe_{0.95}P_{0.05}O_{3-\delta}$ has higher electrical conductivity and better electrocatalytic activity compared to $Ba_{0.95}La_{0.05}FeO_{3-\delta}$. In light of these results, we suggest that nonmetal element doping is an effective strategy for the design of new ferrites.

KEYWORDS: *solid oxide fuel cells, density functional theory, barium ferrite oxide cathode, oxygen reduction reaction, nonmetal element doping*

1. INTRODUCTION

Solid oxide fuel cells (SOFCs) will likely play a major role as the next generation's energy conversion systems because of their low emissions, high efficiencies, and fuel flexibility.[1,2] Despite their considerable promise, SOFCs are still not widely commercialized because of high costs. These costs are mainly due to SOFCs' high operating temperatures, typically between 800 and 1000 °C.[3] Working at these high temperatures imposes strict thermal management requirements and raises the cost of various components.[4] In addition, the higher the temperature, the more severe the performance decay of SOFC materials.[5] Therefore, operating below 800 °C is essential to make the SOFC technology commercially viable.[6] One of the most critical challenges for the operation in the intermediate temperature (IT) range (between 500 and 800 °C) is the sluggish kinetics of the oxygen reduction reaction (ORR).[7,8] Researchers found that mixed ionic−electronic conductors (MIECs), especially perovskite (ABO_3) cathodes,[9] perform well at ITs. Thanks to their capability of conducting both electrons and O ions, MIECs can extend the ORR region to the entire gaselectrode interface, thus providing enlarged active areas compared to conventional materials, which are limited by the triple-phase boundary (TPB), the region where electrolyte, air, and electrode phases meet.[10] Because the structure of perovskites can accommodate various cations in both the A- and B-sites, the material properties can be adjusted by substitution. Therefore, perovskite-based MIECs have attracted significant attention from researchers worldwide.[11−13]

SOFC cathode materials need to have a high O diffusivity, electrical conductivity, and electrochemical activity toward ORR.[14] In the perovskite oxide family, $La_{1-x}Sr_xMnO_{3-\delta}$ (LSM) has been extensively studied because of its high electrical conductivity (~10^2 S/cm) and thermal expansion coefficient (TEC) closely matching that of YSZ, a conventionally used electrolyte.[15] However, the ionic conductivity of LSM is poor, limiting the electrochemically active reaction to the TPB.[9] Moreover, LSM's performance decays quickly when the operating temperature falls below 800 °C.[16] Cobalt-based

Received: March 25, 2019
Accepted: July 22, 2019
Published: July 22, 2019

DOI: 10.1021/acsaem.9b00624
ACS Appl. Energy Mater. 2019, 2, 5472−5480

perovskites, e.g., $La_{1-x}Sr_xCo_{1-y}Fe_yO_{3-\delta}$,[17−20] $Ba_xSr_{1-x}Co_{0.8}Fe_{0.2}O_{3-\delta}$ (BSCF),[21,22] and $SrNb_{0.1}Co_{0.9}O_{3-\delta}$,[23] unlike LSM, are MIECs with considerable promise for IT-SOFCs. Thanks to the presence of Co, they are highly active and able to show excellent ORR activity at temperatures below 800 °C.[9] However, the high cost of Co (36000 USD/ton) (the price of iron is 75 USD/ton) is a major limitation for these materials.[24] Therefore, cobalt-free materials, such as ferrites, are needed.[25] Among ferrites, materials based on cubic $BaFeO_{3-\delta}$ (BF) stand out thanks to their excellent electrochemical activity and stability.[26,27] However, BF ceramics made using conventional techniques consist of two phases: one electrochemically highly active, the cubic phase, and one electrochemically inactive, the hexagonal phase.[28] Experiments have shown that a relatively small substitution of La into the Ba-site renders the material purely cubic.[28,29] Thanks to its high O nonstoichiometry,[30] the resulting material, $Ba_{0.95}La_{0.05}FeO_{3-\delta}$ (BLF), appears to be nearly active as BSCF.[28] In addition to the Ba-site substitution, the cubic phase can also be formed by introducing other transition metal elements, such as Zr, Ca, and Y, in the Fe-site.[27,31−33] However, the electrical conductivity of Fe-site-substituted BF is lower compared to that of Ba-site-substituted BF. The lower conductivity may be ascribed to the redox inactivity of Fe-site dopants in comparison to Fe.[31]

The lower electrical conductivity of Fe-site-substituted BF may be resolved by introducing nonmetal elements. Recently, the Slater group found that incorporation of Si, P, and S into perovskites, such as $SrMO_3$ (M = Co, Mn),[34] $La_{1-y}Sr_yMnO_{3-\delta}$,[35] $SrFeO_{3-\delta}$,[36] and $La_{0.6}Sr_{0.4}Co_{0.8}Fe_{0.2}O_{3-\delta}$,[37] can significantly enhance the electrical conductivity and improve the phase stability. In particular, the incorporation of 5 at. % P in the B-site increases the conductivity of $CaMnO_{3-\delta}$ at 800 °C from 7.6 to 43.0 S cm^{-1} [43] and $SrCoO_{3-\delta}$ at 25 °C from 2 to 312 S cm^{-1}.[38] Furthermore, the area specific resistance (ASR) of the symmetrical cell with $CaMn_{0.95}P_{0.05}O_{3-\delta}$ electrodes is only 0.30 Ω cm^2 at 800 °C, a value 80% smaller than the one reported for pristine $CaMnO_{3-\delta}$ (1.50 Ω cm^2).[35] Additionally, both X-ray diffraction and neutron diffraction suggest that Si, P, and S are located at the B-sites with four coordinating O atoms, i.e., SiO_4, PO_4, and SO_4.[34−37] Compared to the conventional BO_6 octahedral structures, the above-mentioned oxyanion groups have a smaller O coordination number, hereby favoring the presence of O vacancies.[34−37]

Inspired by the great enhancement in electrical conductivity brought by nonmetal element substitution, we explored whether this strategy can be applied more widely to ferrites by studying Ba-based materials. In particular, we first performed density functional theory (DFT) calculations to relax the structures of $Ba_{0.875}La_{0.125}FeO_{3-\delta}$ ($BLF_{0.125}$) and $Ba_{0.875}La_{0.125}Fe_{0.875}P_{0.125}O_{3-\delta}$ ($BLFP_{0.125}$), and we noticed that P substitution has a negligible effect on the crystal structure. We also assessed the O vacancy formation energy and migration barrier based on BF and $BaFe_{0.875}P_{0.125}O_{3-\delta}$ (BFP) without considering La substitution. We found that both energies decrease in BFP compared to BF, suggesting that P-substituted BLF has more O vacancies and faster O diffusion. We further evaluated the structural stability and observed that the PO_4 structure, i.e., P coordinated with four O atoms, is structurally more stable. Later, we experimentally investigated the impact of P substitution on the electronic conductivity and electrochemical activity of BLF. We successfully incorporated 5 at. % of P into the Fe-site of BLF to make $Ba_{0.95}La_{0.05}Fe_{0.95}P_{0.05}O_{3-\delta}$ (BLFP) without detecting secondary phases in the X-ray diffraction (XRD) scans. We also discovered that BLFP's electrical conductivity at 430 °C (~18 S/cm) is 50% higher than that of BLF. Furthermore, the ASR value of BLFP is 85% lower than that of BLF at 700 °C. This work highlights the potential of BLFP as a cathode material for IT-SOFCs. Furthermore, this work proposes the design of new ferrites by P, a nonmetal element, which enables the formation of PO_4 structures within these materials.

2. METHODS

2.1. First-Principles Calculations. The spin-polarized density functional theory (DFT) was conducted by using the Vienna *ab initio* simulation package (VASP).[39] The projector augmented wave (PAW) method[40] was employed, together with the exchange-correlation described by the Perdew−Burke−Ernzerhof (PBE) functional[41] under the generalized gradient approximation (GGA) scheme. The kinetic energy cutoff was set at 475 eV. A DFT+U approach with a U_{eff} value of 4.0 eV[42,43] was used to account for the localized 3d electrons of Fe. The convergence criteria were set at 10^{-5} eV for the energy and 0.02 eV/Å for the force.

Because O vacancies directly affect the ORR performance by enabling ionic transport and providing active sites for ORR, the O vacancy formation energy, $\Delta E_{f,vac}$, is an important metric to characterize the ORR activity. $\Delta E_{f,vac}$ is computed by removing one neutral O atom from the perfect cubic structure, and its value is approximated by using the following equation,[42,44] without considering thermal and vibrational effects:

$$\Delta E_{f,vac} = E_{defective} - E_{defect\text{-}free} + \frac{1}{2}(E_{O_2} + \Delta h_O) \quad (1)$$

where $E_{defective}$ and $E_{defect\text{-}free}$ are the energies of defective and defect-free materials, δ_{O_2} is the energy of an isolated O_2 molecule, and Δh_O (1.36 eV) is the correction term due to O_2 overbinding.[45] According to eq 1, a smaller $\Delta E_{f,vac}$ correlates to lower energetic cost for vacancy formation and, therefore, a higher concentration of O vacancies.[43,44,46]

2.2. Preparation of the Powders and Fabrication of Symmetrical Cells. The BLF and BLFP powders were prepared by a combined EDTA (ethylenediaminetetraacetic acid)−citrate complexing process.[29] The precursors $Ba(NO_3)_2$, $La(NO_3)_3$, $Fe(NO_3)_3$, and $(NH_4)_2HPO_4$ (all in A.R. grade, Sinopharm Chemical Reagent Co. Ltd.) were used as the cationic sources. Stoichiometric amounts of the nitrates listed above were first dissolved in deionized water. Then, EDTA and citric acid were added with a mole ratio of 1:1:2 for total cation ions:EDTA:citric acid. To avoid precipitation, the pH value of the mixture was kept at 6 by adding an NH_3 aqueous solution. Following that, the water in the mixture was evaporated at 120 °C under stirring until a viscous and yellow gel formed. The gel was subsequently placed into an oven at 250 °C for 6 h to produce a dark solid precursor. The obtained precursor was finely ground and, finally, calcined in a furnace at 1200 °C for 5 h in air to remove carbon and form the BLF and BLFP powders.

2.3. Basic Characterizations. We identified the phase structure of the synthesized materials by X-ray diffraction (Philips, X'Pert). The XRD pattern was recorded with Cu Kα radiation (λ = 1.5406 Å, 40 kV, 40 mA) scanning from 15° to 90° (0.02° step). We also characterized the structure evolution of BLFP by high temperature (HT) XRD in air from 100 up to 800 °C with an interval of 100 °C. The HT-XRD scan ranged from 20° to 80° with a step of 0.02° to observe the evolution of the main peaks.

To detect the target elements and analyze the charge state of the cations present in the perovskite, we conducted X-ray photoelectron spectroscopy (XPS) with an instrument (PHI5600) characterized by a monochromatic Al-source X-ray in a vacuum chamber at 10^{-8}−10^{-9} Pa. The charge neutralizer was used during all tests to control the charge of the sample. The XPS scan was conducted from 0 to 1400 eV

DOI: 10.1021/acsaem.9b00624
ACS Appl. Energy Mater. 2019, 2, 5472−5480

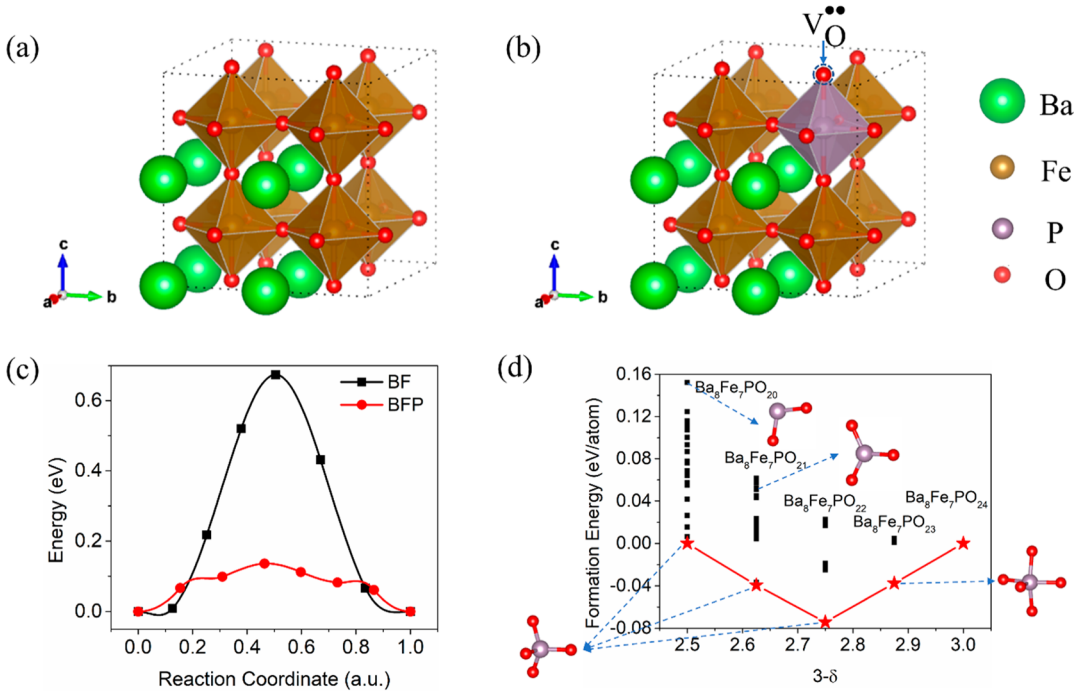

Figure 1. The 2 ×2 × 2 supercells used for the (a) BF and (b) BFP simulations. In (b), the O vacant site with the lowest formation energy is labeled with a circle. (c) Migration barrier for O diffusion in BF and BFP, where the red line corresponds to the diffusion path closest to the P cation. (d) Relative formation energies of BFP at various δ values; the obtained O arrangements around P obtained by relaxing specific compositions are also shown.

with a 1 eV step, and the pass energy was set to 160 eV. To obtain a high-resolution scan of the target elements, the pass energy was decreased to 40 eV and the scanning rate was decreased to 0.1 eV.

At RT, the bulk O nonstoichiometry, δ, was measured via iodometric titration.[31] Thermal gravimetric analysis (TGA, TA Instruments TGA, Q500) was employed to investigate δ as a function of temperature. The sample was heated from RT to 800 °C with a ramping rate of 10 °C/min. Then, the δ at different temperatures was calculated via the following equation:[28]

$$\delta(T) = \frac{Mm_{RT} - (M - 15.9994\delta_{RT})m(T)}{15.9994m_{RT}} \quad (2)$$

where m_{RT} and $m(T)$ are the sample masses at RT and at the given temperature, respectively, M is the molar mass of stoichiometric form of BLFP, i.e., $Ba_{0.95}La_{0.05}Fe_{0.95}P_{0.05}O_3$, and δ_{RT} is the O nonstoichiometry at RT.

2.4. Electrochemical Performance. We employed a four-probe DC method to test the electrical conductivity of the synthesized materials. The sample powders were first ball milled (500 rpm, 90 min) and then compressed into 15 mm × 6 mm × 3 mm bricks. The bricks were then placed into a furnace at 1200 °C for 12 h in air for sintering. Four Ag wires were attached with Ag paste, and the sample was heated at 180 °C to ensure bonding to the sample. Conductivities were measured in a controlled dry air consisting of 21% O_2 and 79% N_2 from 300 to 900 °C with an interval of 20 °C.

We analyzed the bulk diffusion kinetics using the electrical conductivity relaxation (ECR) at 700 °C with the identical setup as the one employed for the electrical conductivity measurement. After the conductivity reading reached equilibrium, the gas fed into the test tube was suddenly switched from pure O_2 to O_2:N_2 = 21:79. The switch of oxygen partial pressure causes a change of O vacancy concentration in the material, which leads to a conductivity that changes over time.

Electrochemical impedance spectroscopy (EIS) measurements were performed to evaluate the ORR activity using a symmetrical two-electrode configuration. The electrodes were prepared by first dispersing the BLF or BLFP powders in a solution of isopropyl alcohol, ethylene glycol, and glycerol. The mixture formed a colloidal suspension thanks to ball milling (500 rpm for 90 min). The suspension was then sprayed on both sides of the 20% Sm-doped CeO_2 (SDC) pellets (diameter ~11 mm). The resulting disks were calcined at 1000 °C for 2 h in air to obtain BLFP|SDC|BLFP symmetrical cells. Finally, Ag paste was used on both sides of the cell as current collectors, and silver wires were attached.

We tested the symmetrical cells in a tube furnace with temperature and atmosphere control. We controlled the partial pressure of O_2 by varying the O_2 and N_2 flow rates. The EIS was measured within a temperature range from 550 to 750 °C with an interval of 50 °C and an O_2 partial pressure range from 0.21 to 1 atm. A VSP Biologic impedance analyzer was used to carry out the potentiostatic EIS with a potential amplitude of 20 mV and frequencies from 100 mHz to 100 kHz.

3. RESULTS AND DISCUSSION

3.1. Simulations. We first conducted structural optimization of $BLF_{0.125}$ and $BLFP_{0.125}$ using a 2 × 2 × 2 supercell consisting of 40 atoms, where the minimum substitution rate of both La and P is 1/8. The relaxed structure of $BLF_{0.125}$ is cubic with a lattice constant of 3.994 Å while $BLFP_{0.125}$ is in quasi-cubic with a lattice constant of 4.000 Å. The two nearly identical values suggest a negligible effect of P doping on the crystal structure of BLF.

To establish the impact of P substitution on the electrocatalytic activity, we performed the following calculations based on BF and BFP (see Figure 1a,b) without considering La substitution. Eliminating La simplifies the computations significantly, and we expect that this approximation still sheds light on understanding the mechanism of substituting Fe with P. We first optimized the structures and observed that both BF and BFP are relaxed to cubic structures with a lattice constant of 4.014 and 4.020 Å, respectively. Consistent with La-substituted ones, introducing P in the Fe-site leads to minor

DOI: 10.1021/acsaem.9b00624
ACS Appl. Energy Mater. 2019, 2, 5472−5480

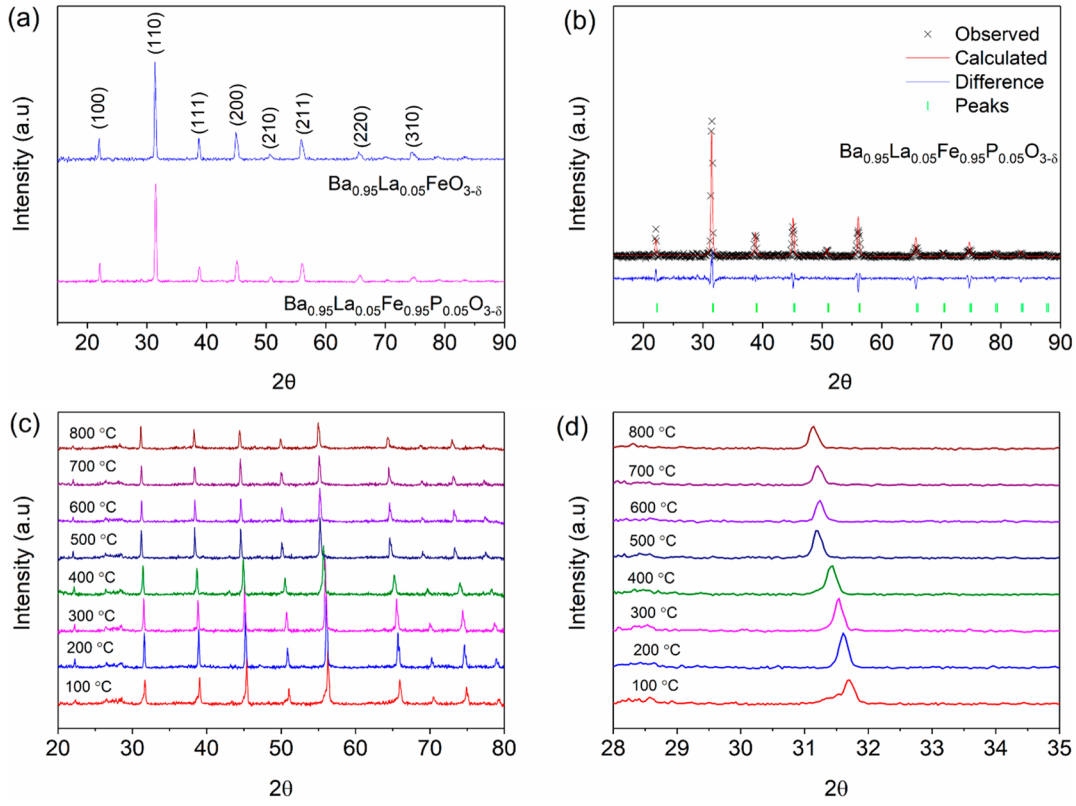

Figure 2. (a) XRD patterns of BLF and BLFP. (b) XRD refinement for BLFP. (c) HT-XRD patterns of BLFP powder up to 800 °C. (d) Magnified HT-XRD pattern of scan range 28°−35°.

changes of crystal structures, and the compression of lattice constants for La-substituted materials is obvious since La has a smaller ionic radius than Ba. We further estimated the $\Delta E_{f,vac}$ values of BF and BFP by removing one neutral O atom. Because of the high symmetry of BF, there is only one unique O vacant site with $\Delta E_{f,vac}$ as 0.83 eV, in agreement with previous calculations.[42,43,47,48] Conversely, there are several unique O vacant sites in BFP. We found that the vacant site nearest to P (see Figure 1b) has the lowest formation energy with a value of −0.25 eV, while forming other vacant sites requires energies comparable to that of BF. Such a conclusion suggests that substituting Fe with P may increase the O nonstoichiometry, hence introducing more O vacant sites.

To assess the impact of the P substitution on the O diffusion, we computed the migration barrier by the climbing image nudged elastic band (CINEB) method. Surprisingly, BFP has a much lower migration barrier compared to pristine BF, as shown in Figure 1c. The calculated O migration barrier for BF is also comparable to those computed for other Fe-based perovskites, such as $Ba_{0.5}Sr_{0.5}Co_{1-y}Fe_yO_{2.875}$[48,49] and $La_{0.5}Sr_{0.5}Co_{1-y}Fe_yO_{2.875}$.[50] The much smaller O vacancy migration barrier in BFP indicates a faster ion transport, suggesting a faster chemical diffusivity of BLFP relative to BLF.

We also evaluated the structural stability of BFP and the coordination of P with O atoms by investigating a series of BFP materials, i.e., δ = 0, 0.125, 0.25, 0.375, and 0.5. The relative formation energies,[51] defined as the energy difference with respect to those of $BaFe_{0.875}P_{0.125}O_3$ and $BaFe_{0.875}P_{0.125}O_{2.5}$, are shown in Figure 1d, where the red stars correspond to the structures with the lowest relative formation energy. As shown above, for δ = 0.125, the O vacancies preferably form near P, leading to a local PO_5 arrangement. For $\delta \geq 0.25$, the most stable BFP structures are those with only two O-sites vacant near P, forming tetrahedral PO_4. If more than two O atoms are removed near P, then all computed energies are above the hull; see dots above the red line in Figure 1d. This implies that if P in BFP is coordinated with four O atoms to give PO_4, the material is more stable.

3.2. Phase Characterization. Figure 2a reports the XRD scan of the synthesized BLF and BLFP. Both materials are in the cubic phase (space group $Pm\bar{3}m$) with no detectable impurities. Rietveld refinement provides the average lattice constants of 4.019 and 4.014 Å for BLF and BLFP, respectively, in qualitative agreement with DFT calculations, and the measured values of BLF also match those obtained previously.[28,31] As proposed by the Slater group, introducing P in the Fe-site can have two opposite effects on the lattice parameters. On the one hand, it can lead to the shrinkage of the lattice parameters due to the smaller radius of P^{5+} and, on the other hand, an expansion because of a partial reduction of Fe^{4+} to Fe^{3+}, which has a larger ionic radius compared to Fe^{4+}.[34−37] The resultant negligible difference in lattice constants suggests that these two effects may balance out and that 5 at. % P substitution has a limited influence on the structure of BLF.

To further examine the thermal stability of BLFP and test its thermal expansion coeffcient (TEC), we conducted HT-XRD measurements (see Figure 2c). BLFP maintains a cubic structure up to 800 °C, suggesting good phase stability of BLFP in air. To further evaluate the material's volume expansion, we magnified the scan between 28° and 35°, as shown in Figure 2d. As the temperature increases, the reflections move to lower angles, indicating a lattice expansion (about 1.97% at 800 °C).[52] The TEC of BLFP is estimated to

DOI: 10.1021/acsaem.9b00624
ACS Appl. Energy Mater. 2019, 2, 5472−5480

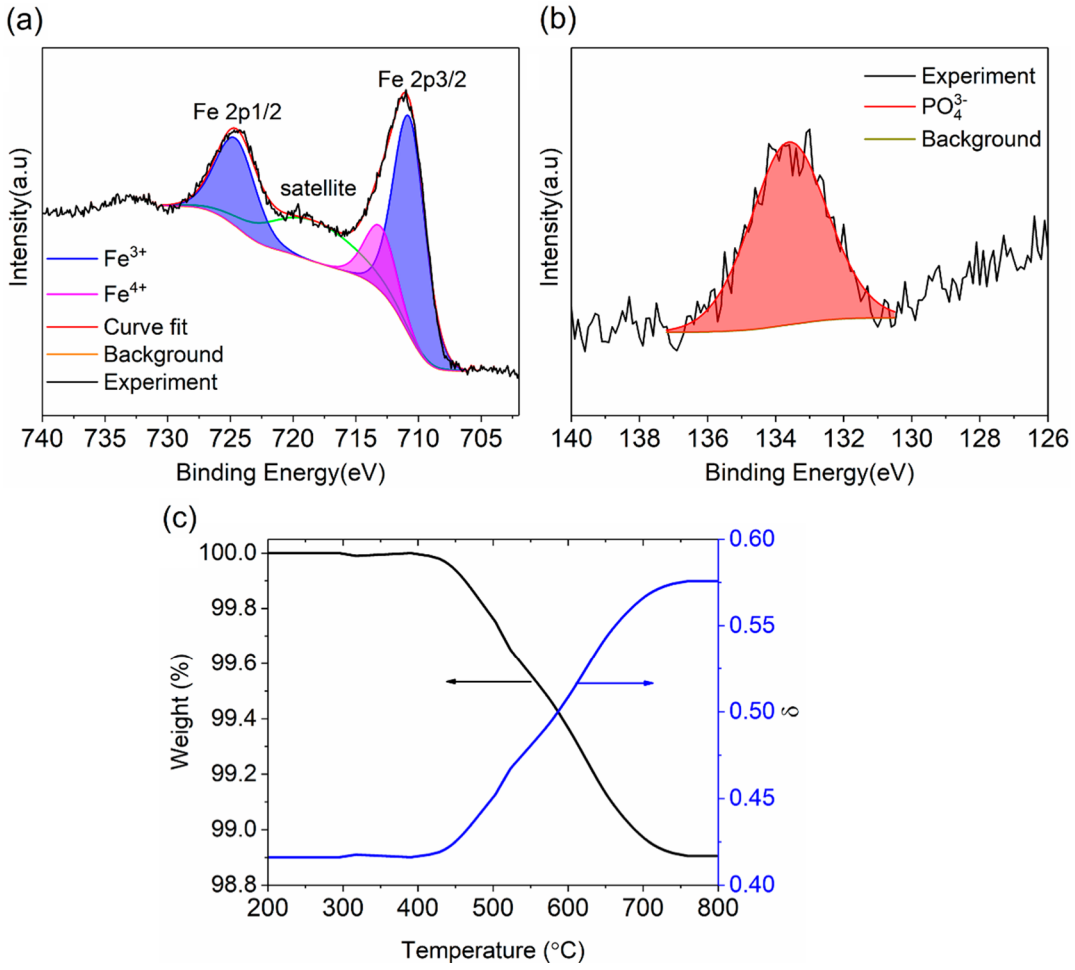

Figure 3. High-resolution XPS scan of the (a) Fe 2p orbital and (b) P 2p orbital in the BLFP. (c) TGA and O nonstoichiometry of BLFP as a function of temperature.

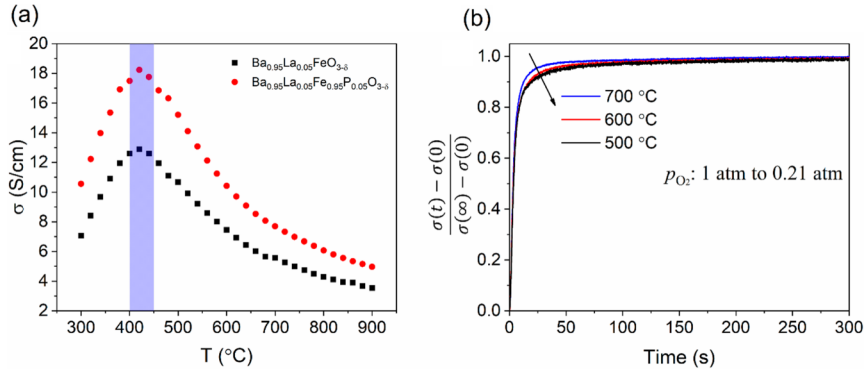

Figure 4. (a) Electrical conductivity of BLF and BLFP at various temperatures and (b) conductivity relaxation of BLFP at 500−700 °C with O_2 partial pressure switched from 1 to 0.21 atm.

be 25.48 × 10^{-6} K^{-1}. Even though BLFP has a higher TEC than the conventional YSZ electrolyte (11.0 × 10^{-6} K^{-1}),[53] its value is comparable to that of the state-of-the-art $Ba_xSr_{1-x}Co_{0.8}Fe_{0.2}O_{3-\delta}$ (20 × 10^{-6} K^{-1}).[22] In addition, the measured TEC is smaller than that of BLF (30.4 × 10^{-6} K^{-1}),[28] implying the P substitution lowers the TEC.

3.3. Composition. To estimate the valence state of Fe and P, we conducted higher resolution XPS scans of the Fe 2p and P 2p orbitals, as shown in Figure 3. The Fe $2p_{3/2}$ and Fe $2p_{1/2}$ peaks are captured in addition to a satellite feature at 718.5 eV. By deconvolving the two main peaks, we obtain subpeaks at 710.7 eV (Fe $2p_{3/2}$) and 724.6 eV (Fe $2p_{1/2}$), corresponding to Fe^{3+}, and a peak at 713.0 eV (Fe $2p_{3/2}$) associated with Fe^{4+}.[54] The Fe^{3+}:Fe^{4+} ratio can be computed by comparing the corresponding areas, and it suggests an average valence state of Fe (3.12), a value slightly lower than the one obtained for BLF (~3.17).[31] The decrease in the charge state of Fe may be attributed to the partial reduction of Fe^{4+} [51,53] linked to the formation of PO_4^{3-}. Consistently, the P 2p orbital can be assigned to PO_4^{3-} (133.6 eV),[35,37] in line with the above

DOI: 10.1021/acsaem.9b00624
ACS Appl. Energy Mater. 2019, 2, 5472−5480

evaluation of structural stability and O coordinating numbers of P. We also estimated the atomic ratio of P by XPS, i.e., [P]/([Ba] + [La] + [Fe] + [P]) = 5.5%, to be higher than the nominal value. However, this value may indicate that the surface of BLFP is Fe-deficient,[55] in agreement with the atomic ratio obtained by EDS mapping.

We also evaluated the oxidation state of Fe by iodometric titration three times. We estimated it to be 3.02, in qualitative agreement with the results from XPS. Iodometric titration predicts the δ value of BLFP to be 0.42, a value higher than that of BLF (0.39),[28,31] in accordance with the prediction of lower O vacancy formation energies for P-substituted materials. The δ at high temperatures was measured by TGA, as illustrated in Figure 3c, where mass loss starts at 450 °C and levels off at 700 °C. Above 700 °C, δ is around 0.57, a value similar to that observed in BLF and $BaFe_{0.95}Zr_{0.05}O_{3-\delta}$.[28,31]

3.4. Electrical Conductivity and ECR. To evaluate the potential of BLFP as a cathode material for SOFCs, we first tested its electrical conductivity (σ) together with that of BLF (see Figure 4a). The conductivity of both materials varies with the temperature and follows the same trend. Below ~430 °C, the conductivity monotonously increases. Above ~430 °C, the conductivity decreases. This trend, in agreement with previous results,[38,43] suggests a semiconductive behavior at low temperature followed by a metallic behavior. The drop of σ may be ascribed to the reduction of Fe^{4+} to Fe^{3+} due to the O loss at ~430 °C, as illustrated by the TGA in Figure 3c. Most importantly, we observe that the substitution of P improves the electrical conductivity significantly. Furthermore, the conductivity of BLFP is comparable to that of the state-of-the-art cathode material $Ba_{0.5}Sr_{0.5}Co_xFe_{1-x}O_{3-\delta}$ (30 S/cm at 300−400 °C).[22,56] This improvement can be attributed to the substitution of Fe with higher valence P^{5+}.[38]

We also tested the ECR performance of BLFP from 500 to 700 °C, as shown in Figure 4b. Consequently, the bulk diffusion D_{chem} and surface exchange coefficient k_{ex} were fitted by the ECRTOOLs software.[57−59] The D_{chem} was calculated to be $(4.95 \pm 0.33) \times 10^{-4}$ cm^2/s at 500 °C, $(5.67 \pm 0.32) \times 10^{-4}$ cm^2/s at 600 °C, and $(2.90 \pm 1.45) \times 10^{-3}$ cm^2/s at 700 °C. Such values are higher than those measured for BLF (3.82×10^{-5} cm^2/s at 700 °C) and $BaFe_{0.95}Zr_{0.05}O_{3-\delta}$ (3.27×10^{-4} cm^2/s at 700 °C).[31] We further obtained k_{ex} at 700 °C as $(1.50 \pm 0.13) \times 10^{-2}$ cm^2/s, which is much higher than that of BLF (8×10^{-4} cm^2/s).[28] The improved performance of BLFP may be attributed to the higher concentration of O vacancies and lower O migration barrier compared to BLF. These conclusions are also supported by the DFT calculations above. Thanks to the quick ECR response, we expect a better ORR catalytic activity of BLFP over BLF.

3.5. Microstructure. In addition to the electrical conductivity, the microstructure of the cathode layer and the contact between the electrode and the electrolyte are critical to the SOFC performance. A suitable SOFC cathode must be highly porous to increase reaction areas and the accessibility of gases.[14] It should also have a small thickness, e.g., 10−30 μm, to reduce the transport resistance of charge carriers.[9] Figure 5 shows the SEM image of the cross section of cathode layer in BLF|SDC|BLF and BLFP|SDC|BLFP symmetrical cells after sintering at 1000 °C for 2 h. We notice that the cathode layer is porous and the thickness is about 25−30 μm for both materials, a value large enough to eliminate the impact of Ag catalytic activity on the electrochemical performance.

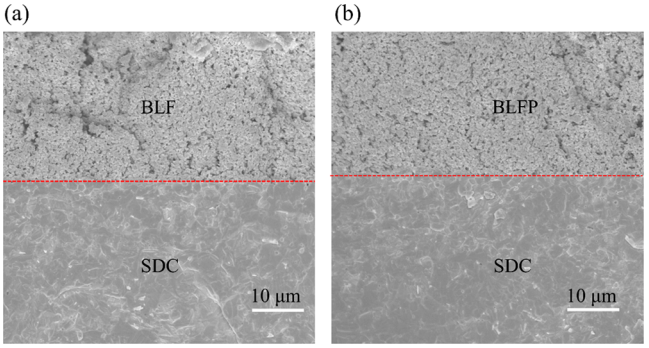

Figure 5. Cross-section SEM images of the cathode layer of (a) BLF and (b) BLFP sintered at 1000 °C for 2 h.

We also identified the composition of the cathode layer by EDS mapping, where a uniform distribution of the target element can be observed. Table 1 lists the atomic ratio of BLFP, where the ratios of Ba/La and Fe/P are 23.6 and 19.8, respectively, in good agreement with the nominal stoichiometry.

Table 1. Atomic Ratio of Elements in the BLFP Cathode Layer from EDS

element	Ba	La	Fe	P	O
atomic ratio (%)	16.5	0.7	15.8	0.8	46.0

3.6. Electrocatalytic Activity. We measured the electrochemical activity of BLF and BLFP using BLF|SDC|BLF and BLFP|SDC|BLFP symmetrical cells. Figure 6a shows the EIS spectra collected at 700 °C. The ASR is obtained by normalizing the polarization resistance (the width of the arc) with respect to the surface area. The ASR value of BLF is quantitively comparable to our previous measurements.[31] Strikingly, the impedance of BLFP is significantly decreased compared to BLF, and the ASR value is only 0.023 Ω cm^2. The lower polarization resistance may be attributed to the improved electrical conductivity, the additional O vacant sites, and the fast diffusion of O vacancies.

The ASR is also shown versus temperature in dry air at p_{O_2} = 0.21 atm, as seen in Figure 6b. According to the Arrhenius law, the activation energy (E_a) at p_{O_2} = 0.21 atm is calculated to be 73.09 and 101.99 kJ/mol for BLF and BLFP, respectively. BLFP's activation energy is larger than that of BLF; however, the E_a value of BLFP is still comparable to (or even smaller) than the E_a reported for other cobalt-free materials, such as $Bi_{0.5}Sr_{0.5}FeO_{3-\delta}$, $La_{0.5}Sr_{0.5}FeO_{3-\delta}$, and $Ba_{0.95}Sm_{0.05}FeO_{3-\delta}$.[31,60,61] Additionally, BLFP's E_a is weakly dependent on p_{O_2}; it only changes to 125.29 kJ/mol at p_{O_2} = 1.0 atm, as seen in Figure 6c.

We also estimated the value of m in the expression $R_p \propto p_{O_2}^{-m}$ [10] to quantitatively assess the ORR rate-limiting step, as seen in Figure 6d. If m = 0.25, the rate-limiting step is the charge transfer process at the gas|electrode interface, following $O_{2ads} + 2e^- + V_O^{\cdot\cdot} \rightleftharpoons 2O_O^X$. For m = 0.5, atomic O mainly limits the oxygen dissociation and the reaction process, $O_{2ads} \rightleftharpoons 2O_{ads}$. At higher temperatures (700−750 °C), m is equal to 0.5, suggesting that the oxygen dissociation process is rate-limiting. When the temperature decreases, m also reduces and reaches 0.25 below 650 °C, indicating that the charge transfer is rate-

DOI: 10.1021/acsaem.9b00624
ACS Appl. Energy Mater. 2019, 2, 5472−5480

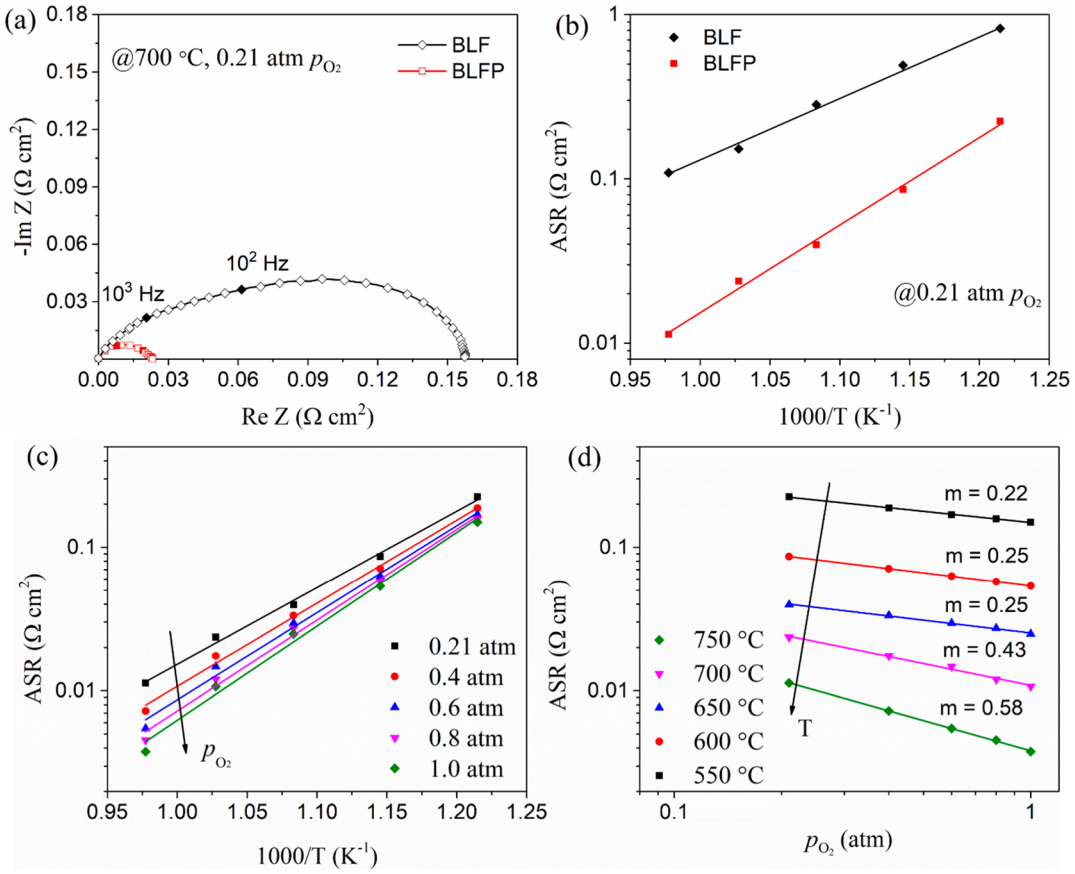

Figure 6. (a) Nyquist plot of the EIS of symmetrical BLF|SDC|BLF and BLFP|SDC|BLFP cells measured at 700 °C with p_{O_2} = 0.21 atm. (b) ASR of BLFP as a function of temperature at p_{O_2} = 0.21 atm. ASR values of BLFP versus (c) the inverse of the temperature and (d) the oxygen partial pressure.

limiting. Such conclusions are also consistent with our previous experiments on BLF.[31]

4. CONCLUSION

By means of DFT calculations, it was predicted that substituting Fe in $Ba_{1-x}La_xFeO_{3-\delta}$ with P lowers both the formation energy of O vacancies and their migration barrier without altering the crystal structure. It was further identified that the coordination of P with O favors the creation of PO_4 groups and the formation of O vacancies. To verify the theoretical conclusions, $Ba_{0.95}La_{0.05}Fe_{0.95}P_{0.05}O_{3-\delta}$ (BLFP) and $Ba_{0.95}La_{0.05}FeO_{3-\delta}$ (BLF) were successfully synthesized by using a combined EDTA−citrate complexing approach. It was observed that it is possible to substitute 5 at. % P in the Fe-site while maintaining the cubic phase structure of BLF. An HT-XRD profile revealed a moderate lattice expansion of BLFP at high temperature. With the introduction of P, a partial of Fe^{4+} species is reduced to Fe^{3+}, together with the creation of O vacancies. XPS results confirmed the reduction of Fe^{4+} with a lower valence state consistently with iodometric titration. Measurements of electrical conductivity and ECR demonstrated that adding a minute amount of P into the Fe-site of BLF improves the material by lowering the polarization resistance of the symmetrical cell, increasing the surface exchange rate and the diffusion coefficients. All these factors are consistent with the DFT predictions and contribute to the improved ORR performance, suggesting that P substitution is an effective approach to design new cathode materials.

AUTHOR INFORMATION

Corresponding Author

*E-mail francesco.ciucci@ust.hk. Phone +852 2358 7187. Fax +852 2358 1543.

ORCID

Jian Wang: 0000-0002-6800-0467

Francesco Ciucci: 0000-0003-0614-5537

Notes

The authors declare no competing financial interest.

ACKNOWLEDGMENTS

The authors gratefully acknowledge the Research Grants Council of Hong Kong for support through the projects (16207615, 16227016, and 16204517). The authors also acknowledge the support from the Guangzhou Science and Technology Program (No. 201807010074). Alessio Belotti acknowledges the support of the Research Grants Council through the Hong Kong Ph.D. Fellowship Scheme.

REFERENCES

(1) Chu, S.; Majumdar, A. Opportunities and challenges for a sustainable energy future. *Nature* **2012**, *488* (7411), 294−303.

(2) Stambouli, A. B.; Traversa, E. Solid oxide fuel cells (SOFCs): a review of an environmentally clean and efficient source of energy. *Renewable Sustainable Energy Rev.* **2002**, *6* (5), 433−455.

(3) Nicholas, J. D. Highlights from the 2013 National Science Foundation Solid Oxide Fuel Cell Promise, Progress, and Priorities

DOI: 10.1021/acsaem.9b00624
ACS Appl. Energy Mater. 2019, 2, 5472−5480

(SOFC-PPP) Workshop. *Electrochem. Soc. Interface* **2013**, *22* (4), 49−54.
(4) Singhal, S. C.; Kendall, K. *High-Temperature Solid Oxide Fuel Cells: Fundamentals, Design and Applications*; Elsevier: 2003.
(5) Wachsman, E. D.; Lee, K. T. Lowering the temperature of solid oxide fuel cells. *Science* **2011**, *334* (6058), 935−939.
(6) Jun, A.; Kim, J.; Shin, J.; Kim, G. Perovskite as a Cathode Material: A Review of its Role in Solid-Oxide Fuel Cell Technology. *ChemElectroChem.* **2016**, *3* (4), 511−530.
(7) Brett, D. J.; Atkinson, A.; Brandon, N. P.; Skinner, S. J. Intermediate temperature solid oxide fuel cells. *Chem. Soc. Rev.* **2008**, *37* (8), 1568−78.
(8) Zhang, Z.; Wang, J.; Chen, Y.; Tan, S.; Shao, Z.; Chen, D. In situ formation of a 3D core-shell and triple-conducting oxygen reduction reaction electrode for proton-conducting SOFCs. *J. Power Sources* **2018**, *385*, 76−83.
(9) Adler, S. B. Factors governing oxygen reduction in solid oxide fuel cell cathodes. *Chem. Rev.* **2004**, *104* (10), 4791−4844.
(10) Liu, J.; Ciucci, F. Modeling the impedance spectra of mixed conducting thin films with exposed and embedded current collectors. *Phys. Chem. Chem. Phys.* **2017**, *19* (38), 26310−26321.
(11) Tsipis, E. V.; Kharton, V. V. Electrode materials and reaction mechanisms in solid oxide fuel cells: a brief review. *J. Solid State Electrochem.* **2008**, *12* (11), 1367−1391.
(12) Richter, J.; Holtappels, P.; Graule, T.; Nakamura, T.; Gauckler, L. J. Materials design for perovskite SOFC cathodes. *Monatsh. Chem.* **2009**, *140* (9), 985−999.
(13) Bu, Y.; Jang, H.; Gwon, O.; Kim, S. H.; Joo, S. H.; Nam, G.; Kim, S.; Qin, Y.; Zhong, Q.; Kwak, S. K.; Cho, J.; Kim, G. Synergistic interaction of perovskite oxides and N-doped graphene in versatile electrocatalyst. *J. Mater. Chem. A* **2019**, *7* (5), 2048−2054.
(14) Sun, C.; Hui, R.; Roller, J. Cathode materials for solid oxide fuel cells: a review. *J. Solid State Electrochem.* **2010**, *14* (7), 1125−1144.
(15) Mizusaki, J.; Yonemura, Y.; Kamata, H.; Ohyama, K.; Mori, N.; Takai, H.; Tagawa, H.; Dokiya, M.; Naraya, K.; Sasamoto, T. Electronic conductivity, Seebeck coefficient, defect and electronic structure of nonstoichiometric La1- xSrxMnO3. *Solid State Ionics* **2000**, *132* (3−4), 167−180.
(16) Minh, N. Q.; Takahashi, T. *Science and Technology of Ceramic Fuel Cells*; Elsevier: 1995.
(17) Tai, L.-W.; Nasrallah, M.; Anderson, H.; Sparlin, D.; Sehlin, S. Structure and electrical properties of La1- xSrxCo1- yFeyO3. Part 1. The system La0. 8Sr0. 2Co1- yFeyO3. *Solid State Ionics* **1995**, *76* (3−4), 259−271.
(18) Esquirol, A.; Brandon, N.; Kilner, J.; Mogensen, M. Electrochemical characterization of La0. 6Sr0. 4Co0. 2Fe0.8O3 cathodes for intermediate-temperature SOFCs. *J. Electrochem. Soc.* **2004**, *151* (11), A1847−A1855.
(19) Murray, E. P.; Sever, M.; Barnett, S. Electrochemical performance of (La, Sr)(Co, Fe)O3−(Ce, Gd)O3 composite cathodes. *Solid State Ionics* **2002**, *148* (1−2), 27−34.
(20) Tai, L.-W.; Nasrallah, M.; Anderson, H.; Sparlin, D.; Sehlin, S. Structure and electrical properties of La1- xSrxCo1- yFeyO3. Part 2. The system La1- xSrxCo0. 2Fe0. 8O3. *Solid State Ionics* **1995**, *76* (3−4), 273−283.
(21) Shao, Z.; Haile, S. M. A high-performance cathode for the next generation of solid-oxide fuel cells. *Nature* **2004**, *431* (7005), 170−173.
(22) Zhou, W.; Ran, R.; Shao, Z. Progress in understanding and development of Ba0. 5Sr0. 5Co0. 8Fe0. 2O3- δ-based cathodes for intermediate-temperature solid-oxide fuel cells: A review. *J. Power Sources* **2009**, *192* (2), 231−246.
(23) Zhou, W.; Shao, Z.; Ran, R.; Jin, W.; Xu, N. A novel efficient oxide electrode for electrocatalytic oxygen reduction at 400−600 C. *Chem. Commun.* **2008**, No. 44, 5791−5793.
(24) Yokokawa, H.; Tu, H.; Iwanschitz, B.; Mai, A. Fundamental mechanisms limiting solid oxide fuel cell durability. *J. Power Sources* **2008**, *182* (2), 400−412.
(25) Bu, Y.-f.; Zhong, Q.; Chen, D.-C.; Chen, Y.; Lai, S. Y.; Wei, T.; Sun, H.-b.; Ding, D.; Liu, M. A high-performance, cobalt-free cathode for intermediate-temperature solid oxide fuel cells with excellent CO_2 tolerance. *J. Power Sources* **2016**, *319*, 178−184.
(26) Teraoka, Y.; Shimokawa, H.; Kang, C. Y.; Kusaba, H.; Sasaki, K. Fe-based perovskite-type oxides as excellent oxygen-permeable and reduction-tolerant materials. *Solid State Ionics* **2006**, *177* (26−32), 2245−2248.
(27) Wang, J.; Lam, K. Y.; Saccoccio, M.; Gao, Y.; Chen, D.; Ciucci, F. Ca and In co-doped BaFeO3- δ as a cobalt-free cathode material for intermediate-temperature solid oxide fuel cells. *J. Power Sources* **2016**, *324*, 224−232.
(28) Dong, F.; Chen, D.; Chen, Y.; Zhao, Q.; Shao, Z. La-doped BaFeO3-δ perovskite as a cobalt-free oxygen reduction electrode for solid oxide fuel cells with oxygen-ion conducting electrolyte. *J. Mater. Chem.* **2012**, *22* (30), 15071−15079.
(29) Chen, D.; Chen, C.; Dong, F.; Shao, Z.; Ciucci, F. Cobalt-free polycrystalline Ba0.95La0.05FeO3-δ thin films as cathodes for intermediate-temperature solid oxide fuel cells. *J. Power Sources* **2014**, *250*, 188−195.
(30) Kida, T.; Yamasaki, A.; Watanabe, K.; Yamazoe, N.; Shimanoe, K. Oxygen-permeable membranes based on partially B-site substituted BaFe 1- y M y O 3- δ (M = Cu or Ni). *J. Solid State Chem.* **2010**, *183* (10), 2426−2431.
(31) Wang, J.; Saccoccio, M.; Chen, D.; Gao, Y.; Chen, C.; Ciucci, F. The effect of A-site and B-site substitution on BaFeO 3-δ: An investigation as a cathode material for intermediate-temperature solid oxide fuel cells. *J. Power Sources* **2015**, *297*, 511−518.
(32) Zhao, H.; Teng, D.; Zhang, X.; Zhang, C.; Li, X. Structural and electrochemical studies of Ba0. 6Sr0. 4Co1- yTiyO3- δ as a new cathode material for IT-SOFCs. *J. Power Sources* **2009**, *186* (2), 305−310.
(33) Liu, X.; Zhao, H.; Yang, J.; Li, Y.; Chen, T.; Lu, X.; Ding, W.; Li, F. Lattice characteristics, structure stability and oxygen permeability of BaFe 1- x Y x O 3- δ ceramic membranes. *J. Membr. Sci.* **2011**, *383* (1), 235−240.
(34) Hancock, C. A.; Slater, P. R. Synthesis of silicon doped SrMO3 (M = Mn, Co): stabilization of the cubic perovskite and enhancement in conductivity. *Dalton transactions* **2011**, *40* (20), 5599−603.
(35) Porras-Vazquez, J. M.; Kemp, T. F.; Hanna, J. V.; Slater, P. R. Synthesis and characterisation of oxyanion-doped manganites for potential application as SOFC cathodes. *J. Mater. Chem.* **2012**, *22* (17), 8287−8293.
(36) Porras-Vazquez, J. M.; Pike, T.; Hancock, C. A.; Marco, J. F.; Berry, F. J.; Slater, P. R. Investigation into the effect of Si doping on the performance of SrFeO3-δ SOFC electrode materials. *J. Mater. Chem. A* **2013**, *1* (38), 11834−11841.
(37) Porras-Vazquez, J. M.; Slater, P. R. Synthesis and Characterization of Oxyanion-Doped Cobalt Containing Perovskites. *Fuel Cells* **2012**, *12* (6), 1056−1063.
(38) Zhu, Y.; Zhou, W.; Sunarso, J.; Zhong, Y.; Shao, Z. Phosphorus-Doped Perovskite Oxide as Highly Efficient Water Oxidation Electrocatalyst in Alkaline Solution. *Adv. Funct. Mater.* **2016**, *26* (32), 5862−5872.
(39) Kresse, G.; Furthmüller, J. Efficient iterative schemes for ab initio total-energy calculations using a plane-wave basis set. *Phys. Rev. B: Condens. Matter Mater. Phys.* **1996**, *54* (16), 11169.
(40) Blöchl, P. E. Projector augmented-wave method. *Phys. Rev. B: Condens. Matter Mater. Phys.* **1994**, *50* (24), 17953.
(41) Perdew, J. P.; Burke, K.; Ernzerhof, M. Generalized gradient approximation made simple. *Phys. Rev. Lett.* **1996**, *77* (18), 3865.
(42) Baiyee, Z. M.; Chen, C.; Ciucci, F. A DFT+U study of A-site and B-site substitution in BaFeO3-delta. *Phys. Chem. Chem. Phys.* **2015**, *17* (36), 23511−23520.
(43) Chen, C.; Ciucci, F. Designing Fe-Based Oxygen Catalysts by Density Functional Theory Calculations. *Chem. Mater.* **2016**, *28* (19), 7058−7065.
(44) Ritzmann, A. M.; Muñoz-García, A. B.; Pavone, M.; Keith, J. A.; Carter, E. A. Ab Initio DFT+U Analysis of Oxygen Vacancy

DOI: 10.1021/acsaem.9b00624
ACS Appl. Energy Mater. 2019, 2, 5472−5480

Formation and Migration in La1-xSrxFeO3-δ (x = 0, 0.25, 0.50). *Chem. Mater.* **2013**, *25* (15), 3011−3019.
(45) Wang, L.; Maxisch, T.; Ceder, G. Oxidation energies of transition metal oxides within theGGA+Uframework. *Phys. Rev. B: Condens. Matter Mater. Phys.* **2006**, *73* (19), 195107.
(46) Kuklja, M.; Kotomin, E. A.; Merkle, R.; Mastrikov, Y. A.; Maier, J. Combined theoretical and experimental analysis of processes determining cathode performance in solid oxide fuel cells. *Phys. Chem. Chem. Phys.* **2013**, *15* (15), 5443−5471.
(47) Mastrikov, Y. A.; Kuklja, M. M.; Kotomin, E. A.; Maier, J. First-principles modelling of complex perovskite (Ba1-xSrx)(Co1-yFey)-O3-δ for solid oxide fuel cell and gas separation membrane applications. *Energy Environ. Sci.* **2010**, *3* (10), 1544−1550.
(48) Merkle, R.; Mastrikov, Y. A.; Kotomin, E. A.; Kuklja, M. M.; Maier, J. First principles calculations of oxygen vacancy formation and migration in Ba1- xSrxCo1- yFeyO3- δ Perovskites. *J. Electrochem. Soc.* **2011**, *159* (2), B219−B226.
(49) Kotomin, E. A.; Mastrikov, Y. A.; Kuklja, M. M.; Merkle, R.; Roytburd, A.; Maier, J. First principles calculations of oxygen vacancy formation and migration in mixed conducting Ba0.5Sr0.5Co1-yFeyO3-δ perovskites. *Solid State Ionics* **2011**, *188* (1), 1−5.
(50) Mastrikov, Y. A.; Merkle, R.; Kotomin, E. A.; Kuklja, M. M.; Maier, J. Formation and migration of oxygen vacancies in La(1-x)Sr(x)Co(1-y)Fe(y)O(3-delta) perovskites: insight from ab initio calculations and comparison with Ba(1-x)Sr(x)Co(1-y)Fe(y)O(3-delta). *Phys. Chem. Chem. Phys.* **2013**, *15* (3), 911−8.
(51) Tuoc, V. N.; Huan, T. D. Predicted Binary Compounds of Tin and Sulfur. *J. Phys. Chem. C* **2018**, *122* (30), 17067−17072.
(52) Chen, Y.; Fong, D. D.; Herbert, F. W.; Rault, J.; Rueff, J.-P.; Tsvetkov, N.; Yildiz, B. Modified Oxygen Defect Chemistry at Transition Metal Oxide Heterostructures Probed by Hard X-ray Photoelectron Spectroscopy and X-ray Diffraction. *Chem. Mater.* **2018**, *30* (10), 3359−3371.
(53) Hayashi, H.; Saitou, T.; Maruyama, N.; Inaba, H.; Kawamura, K.; Mori, M. Thermal expansion coefficient of yttria stabilized zirconia for various yttria contents. *Solid State Ionics* **2005**, *176* (5−6), 613−619.
(54) Yamashita, T.; Hayes, P. Analysis of XPS spectra of Fe2+ and Fe3+ ions in oxide materials. *Appl. Surf. Sci.* **2008**, *254* (8), 2441−2449.
(55) Chen, C.; Chen, D.; Gao, Y.; Shao, Z.; Ciucci, F. Computational and experimental analysis of Ba0.95La0.05FeO3-δ as a cathode material for solid oxide fuel cells. *J. Mater. Chem. A* **2014**, *2* (34), 14154−14163.
(56) Jung, J.-I.; Misture, S. T.; Edwards, D. D. Oxygen stoichiometry, electrical conductivity, and thermopower measurements of BSCF (Ba0.5Sr0.5CoxFe1-xO3-δ, $0 \leq x \leq 0.8$) in air. *Solid State Ionics* **2010**, *181* (27−28), 1287−1293.
(57) Ciucci, F. Electrical conductivity relaxation measurements: Statistical investigations using sensitivity analysis, optimal experimental design and ECRTOOLS. *Solid State Ionics* **2013**, *239*, 28−40.
(58) Ciucci, F. A statistical perspective on oxygen diffusion and surface exchange experiments: Sensitivity analysis, parameter estimation and robust optimal experimental design. *Solid State Ionics* **2013**, *232*, 97−105.
(59) Effat, M. B.; Quattrocchi, E.; Wan, T. H.; Saccoccio, M.; Belotti, A.; Ciucci, F. Electrical Conductivity Relaxation in the Nonlinear Regime. *J. Electrochem. Soc.* **2017**, *164* (14), F1671−F1689.
(60) Ding, H.; Xue, X. Cobalt-free layered perovskite GdBaFe2O5+x as a novel cathode for intermediate temperature solid oxide fuel cells. *J. Power Sources* **2010**, *195* (15), 4718−4721.
(61) Niu, Y.; Sunarso, J.; Liang, F.; Zhou, W.; Zhu, Z.; Shao, Z. A comparative study of oxygen reduction reaction on Bi-and La-doped SrFeO3- δ perovskite cathodes. *J. Electrochem. Soc.* **2011**, *158* (2), B132−B138.

DOI: 10.1021/acsaem.9b00624
ACS Appl. Energy Mater. 2019, 2, 5472−5480